

Noncrystallographic Atomic Arrangement Driven Enhancement of the Catalytic Activity of Au Nanoparticles

Valeri Petkov,^{*,†} Youngmin Lee,[‡] Shouheng Sun,[‡] and Yang Ren[§]

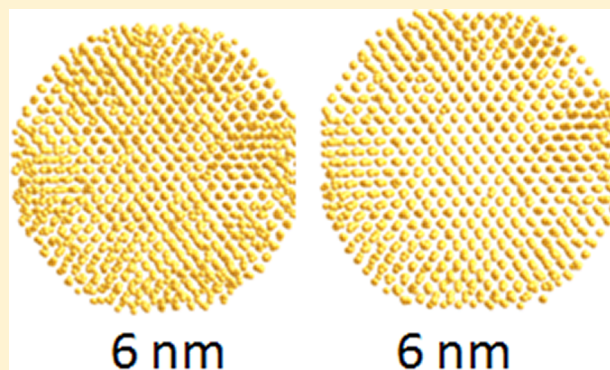
[†]Department of Physics, Central Michigan University, Mt. Pleasant, Michigan 48859, United States

[‡]Department of Chemistry, Brown University, Providence, Rhode Island 02912, United States

[§]Advanced Photon Source, Argonne National Laboratory, Argonne, Illinois 60439, United States

S Supporting Information

ABSTRACT: Determining the atomic-scale structure of nanosized particles remains a challenge and crucial goal for today's science and technology. We investigate the atomic-scale structure of 3–8 nm Au particles obtained by a fast solution reaction and find it to be of a noncrystallographic icosahedral type, in particular, close to the particles' surface. This noncrystallographic structure may well explain the previously observed but poorly understood enhancement of the particles' catalytic properties. Our finding demonstrates that together with size the structure type of nanosized particles can be used as a tunable parameter for achieving improved functionality.



1. INTRODUCTION

The production of countless industrially important materials involves catalysis. Currently, catalysis research is focusing on nanoparticles (NPs) because they show a greatly improved activity. It is believed that the improvement is mostly due to the largely increased NPs' surface-to-volume ratio.^{1–3} Evidence is mounting, however, that nanosized catalysts exhibit a great deal of atomic-scale structural diversity, and this too may affect their catalytic properties substantially.⁴ Clearly, future progress in catalysis research and, hence, many branches of industry depends critically on the ability to obtain precise knowledge about the atomic arrangement in nanosized catalysts. Here we show how high-energy X-ray diffraction (XRD) coupled to atomic pair distribution function (PDF) analysis and computer simulations can accomplish this task with success. In particular, we investigate 3–8 nm Au particles obtained from a fast solution-phase reaction. We find that they possess a heavily distorted atomic-scale structure that departs substantially from the face-centered cubic (fcc)-type ordering exhibited by bulk Au and Au NPs subjected to extra postsynthesis treatment. The distortion is such that atoms close to the surface of the as-synthesized NPs are arranged in a noncrystallographic, icosahedral-type pattern. The icosahedral atomic arrangement concurs with a substantial enhancement of the catalytic activity for oxygen reduction reaction (ORR) in alkaline (KOH) environment.⁵ Our finding provides a vivid example of how, together with size, the structure type can be used to fine-tune useful properties of NPs.

2. EXPERIMENTAL SECTION

2.1. Samples Preparation. The Au NPs studied here were prepared by a solution-phase reaction involving mixing in appropriate proportions of tetrahydronaphthalene (tetralin), oleylamine, and $\text{HAuCl}_4 \cdot 3\text{H}_2\text{O}$ at first. Then, *tert*-butylamine borane (TBAB) and oleylamine in tetralin were mixed by sonication and quickly injected into the above solution. This resulted in very fast NPs nucleation and formation. The resulted Au NPs were precipitated by ethanol addition and collected by centrifugation. NPs with sizes of 3, 6, and 8 nm were obtained by varying the TBAB injection temperature between 276 and 313 K, where the higher the temperature of the reaction the smaller the size of NPs obtained. Oleylamine molecules were used as NPs capping agents. Those molecules were easily removed from the NPs' surface by washing with ethanol and by the alkaline solution used in the tests of the catalytic activity for ORR. In other words, no special higher temperature or other treatment was necessary to obtain clean and catalytically active surface of the as-synthesized Au NPs.

As a control sample, 6 nm Au NPs with a higher degree of crystallinity were also prepared from composite Au– Fe_3O_4 NPs by controlled etching of Fe_3O_4 with H_2SO_4 . The composite Au– Fe_3O_4 NPs were prepared by mixing presynthesized 6 nm Au NPs with a solution of 1-octadecene, oleic acid, and oleylamine. Then, $\text{Fe}(\text{CO})_5$ was injected into the solution. The solution was heated to 300 °C, cooled to room temperature,

Received: October 17, 2012

Revised: November 20, 2012

Published: November 29, 2012

and exposed to air to form Au–Fe₃O₄ nanocomposite particles. They were precipitated by centrifugation. The higher temperature required for the synthesis of the Au–Fe₃O₄ nanocomposite led to the formation of Au nanocrystals.

For the catalytic measurements, Au and Au–Fe₃O₄ NPs were deposited on amorphous carbon support to prevent aggregation. Carbon-supported 6 nm Au–Fe₃O₄ NPs were further treated with H₂SO₄ to remove the iron oxide. The acid etching did not change the size and shape of these 6 nm Au NPs. However, as described below, their atomic-scale structure and catalytic activity changed substantially, indicating a strong synthesis conditions–atomic-scale structure type–functional properties relationship. More details of the preparation conditions can be found in ref 5.

2.2. Transition Electron Microscopy Characterization.

The size and shape of the as-synthesized and etched Au NPs were determined by transition electron microscopy (TEM). Samples for TEM analysis were prepared by depositing and drying a single drop of diluted Au NPs dispersion in hexane on amorphous carbon-coated copper grids under ambient condition. Images were obtained on a Philips EM 420 (120 kV). TEM images (see Figures S1 and S2 of the Supporting Information) showed that the NPs studied here are spherical in shape and highly monodisperse with average sizes of 3.0(5), 6.0(5), and 8.0(5) nm.

2.3. Catalytic Activity Measurements. For the catalytic activity measurement, both as-synthesized 3, 6, and 8 nm NPs and etched 6 nm NPs were deposited on fine carbon powder. The measurements were performed on a Pine Electrochemical Analyzer employing the typical cyclic voltammetry technique. Hg/HgO and Pt wire were used as reference and counter electrodes, respectively. The reaction was carried out in 0.5 M KOH solution. ORR was monitored by changing the rotation speed from 400 to 2500 rpm (rotation per minute) under O₂ saturation conditions.

To compare the catalytic activity of the different samples, we show ORR curves at the same disk rotation speed of 1600 rpm in Figure S3A of the Supporting Information. ORR curves for commercial 5 and 10 nm Au particles are shown as well. Data in Figure S3 of the Supporting Information show that the 3–8 nm Au NPs are more catalytically active for ORR than the commercial Au NPs.⁵ Among the as-synthesized 3–8 nm particles, the 3 nm ones showed a better onset potential for ORR than the 6 nm NPs. This may be expected because the 3 nm particles have a larger surface-to-volume ratio than the 6 nm particles. The 8 nm Au particles, however, showed best catalytic properties, indicating that besides size other factors are important for the enhanced catalytic activity. This was confirmed by the fact⁵ that 6 nm etched NPs showed less catalytic activity as compared with the as-synthesized 6 nm Au particles. (See Figure S3B of the Supporting Information.) To reveal the origin of the different catalytic activity of these Au NPs, we determined their atomic-scale structure by high-energy XRD coupled to atomic PDFs analysis and computer simulations.

2.4. High-Energy Synchrotron X-ray Diffraction.

Synchrotron XRD experiments were carried out under ambient conditions at the 11-ID-C beamline at the Advanced Photon Source using X-rays with energy of 115.232 keV ($\lambda = 0.1076 \text{ \AA}$) and a large-area detector. Synchrotron radiation X-rays were used for two reasons. First, the higher flux of synchrotron radiation X-rays makes it possible to measure the rather diffuse diffraction patterns of Au NPs with a very good statistical

accuracy. Second, the higher energy of synchrotron radiation X-rays makes it possible to reach higher wavevectors, Q , which is essential for the atomic PDF analysis.^{6,7} With the present experiments, diffraction data were collected to wave vectors as high as 30 \AA^{-1} . Experimental XRD patterns are shown in Figure S4 of the Supporting Information. The XRD patterns show broad diffraction features, a picture typical for nanosized materials. Among all samples, the XRD pattern for the etched NPs shows the sharpest diffraction features, indicating an increased degree of crystallinity, yet all diffraction patterns are very diffuse in nature, rendering traditional XRD structure determination inapplicable. That is why we employed the Fourier counterparts of the XRD patterns, the so-called atomic PDFs $G(r)$, which are much better suited for the job.^{6–8}

2.5. Atomic Pair Distribution Function Analysis. In brief, the frequently used atomic PDF $G(r)$ is defined as $G(r) = 4\pi[\rho(r) - \rho_0]$, where $\rho(r)$ and ρ_0 are the local and average atomic number densities, respectively, and r is the radial distance. $G(r)$ peaks at characteristic distances separating pairs of atoms and thus reflects the atomic-scale structure of the material studied. The PDF $G(r)$ is the Fourier transform of the experimentally observable total structure function, $S(Q)$, that is,

$$G(r) = (2/\pi) \int_{Q=Q_{\min}}^{Q_{\max}} Q[S(Q) - 1] \sin(Qr) dQ \quad (1)$$

where Q is the magnitude of the wave vector ($Q = 4\pi \sin\theta/\lambda$), 2θ is the angle between the incoming and outgoing radiation beams, and λ is the wavelength of the radiation used. Note that the structure function, $S(Q)$, is related to only the coherent/elastic part of the scattered X-ray intensities, $I^{\text{coh}}(Q)$, as follows:

$$S(Q) = 1 + [I^{\text{coh}}(Q) - \sum c_i |f_i(Q)|^2] / \sum c_i |f_i(Q)|^2 \quad (2)$$

where c_i and $f_i(Q)$ are the atomic concentration and X-ray scattering factor, respectively, for the atomic species of type i . The great advantage of atomic PDFs in studying materials of a limited length of structural coherence is that the total scattering, including Bragg scattering as well as diffuse scattering, is taken into account. In this way, both the average (i.e., longer-range) atomic-scale structure, manifested in the Bragg-like peaks, and local structural distortions, manifested in the diffuse component of the XRD pattern, are reflected in the PDF. Also, atomic PDFs do not imply any periodicity and therefore can be used to test and refine structure models for materials showing any degree of structural coherence, including models that go beyond the constraints of the 14 Bravais lattices that are used for bulk crystalline materials.

3. RESULTS AND DISCUSSION

Experimental atomic PDFs are shown in Figure 1. All show a series of sharp peaks reflecting the presence of well-defined atomic coordination spheres in 3–8 nm Au NPs. The experimental PDFs, however, decay to zero at distances shorter than the NPs size (e.g., at 2 nm for the 3 nm particles and at 4 nm for the 6 nm particles), indicating the presence of substantial local structural disorder. Both metallic⁶ and nonmetallic⁸ NPs are often found to show such disorder mostly due to surface relaxation effects. The first peak in the experimental PDFs for the as-synthesized Au NPs is positioned at 2.88 \AA , whereas that for the etched 6 nm Au NPs is positioned at 2.86 \AA , indicating that atoms in the latter are

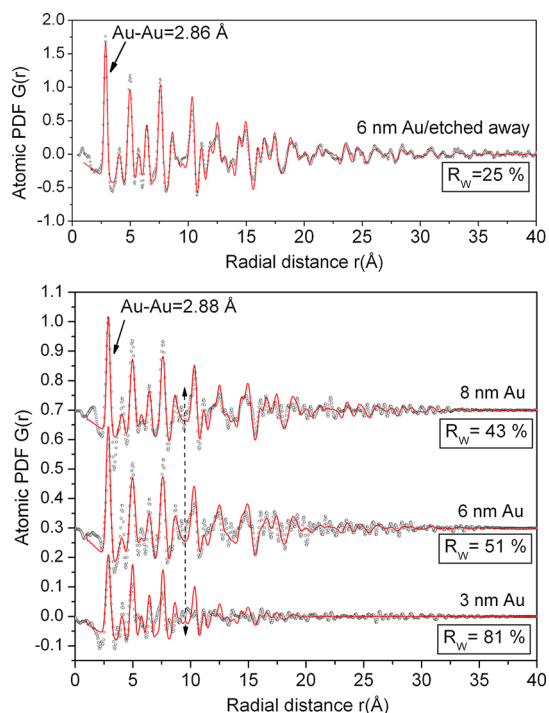


Figure 1. Experimental (symbols) and fcc-constrained model (line) atomic PDFs for 3–8 nm Au particles. That for the etched sample may be well-fit with a model based on the fcc structure of bulk Au. The PDFs for the as-synthesized samples may not be well-fit with a model based on the fcc structure of bulk Au. The respective goodness-of-fit indicators, R_w , are reported by each data set. Arrows mark the Au–Au bond lengths in the two sets of samples. Broken line marks PDFs features that are inconsistent with the fcc-type atomic ordering.

more closely packed than atoms in the former. For reference, the first atomic neighbor distance in bulk Au is 2.88 Å.⁹

The experimental PDFs were first approached with a model based on the fcc-type lattice occurring in bulk Au.⁹ In this type of traditional crystallography constrained modeling,¹⁰ a PDF for an infinite fcc lattice is first computed. Then, each of the coordination spheres of the perfect lattice is broadened by a convolution with a Gaussian function to take into account the presence of thermal (i.e., Debye–Waller type) and static local atomic displacements in NPs. At the same time, the computed

PDF is multiplied by a particle shape (spherical in our case)-dependent function that is zero for distances longer than the size of the NPs being modeled. It is a simplistic approximation to the structure of real NPs but is useful because it allows verifying the type of their atomic arrangement. Data from literature sources for the fcc crystal structures of bulk Au were used as starting values in the PDF fitting. The lattice parameters of the cubic unit cell and atomic isotropic thermal parameters were refined as to minimize a goodness-of-fit indicator, R_w , defined as:

$$R_w = \left\{ \frac{\sum w_i (G_i^{\text{exp}} - G_i^{\text{calc.}})^2}{\sum w_i (G_i^{\text{exp}})^2} \right\}^{1/2} \quad (3)$$

where $G^{\text{exp.}}$ and $G^{\text{calc.}}$ are the experimental and calculated PDFs, respectively, and w_i are weighting factors reflecting the statistical quality of the individual data points. Here it may be added that the best possible agreement factors achieved with the PDF fits are usually in the range of 10–20%, as is the case with the present PDF fits for 6 nm etched away Au NPs (e.g., see the upper panel in Figure 1). Such R_w values appear somewhat high when compared with goodness-of-fit factors resulted from traditional (e.g., Rietveld) analysis of XRD data in reciprocal space. This mostly reflects the fact that the atomic PDFs being fit take both the sharp, Bragg-like features and the diffuse component of the XRD data into account while traditional XRD data analysis considers only the former. The inherently higher absolute value of the goodness-of-fit factors in PDFs fits, however, does not affect their functional purpose as a residuals quantity that guides the refinement of the parameters of the tested structure models and so allows differentiating between them.

As can be seen in Figure 1, the experimental PDFs for as-synthesized 3–8 nm Au particles are poorly approximated by the fcc lattice-constrained model PDFs. In particular, the intensity of several PDFs peaks is badly missed, and some significant PDF features, for example, a peak positioned at ~10 Å (see the broken line in Figure 1), are not captured by the model PDFs at all. The experimental PDF for etched 6 nm Au particles is very well-approximated by this model, indicating that, contrary to the as-synthesized NPs, the etched NPs may be considered as nanosized pieces of the fcc lattice with some surface atomic disorder.

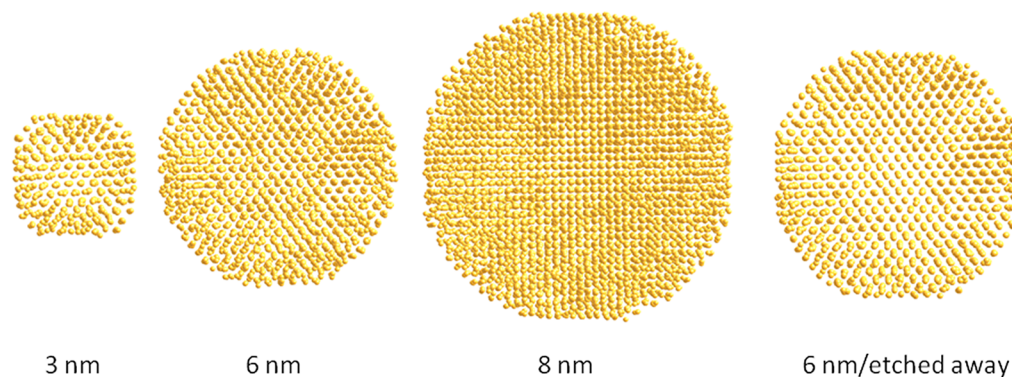


Figure 2. Structure models for 3–8 nm Au particles resulted from the RMC simulations. Note that the models represent assembly averaged structural features of all particles sampled by the X-ray beam (1 mm × 1 mm in the present experiments). In a way, the structure models generated by traditional powder XRD represent an assembly average of all crystallites sampled by the X-ray beam (again typically with a few mm² footprint) employed in those experiments. Comparing particles' assembly averaged structure models to particles' assembly averaged physicochemical properties (e.g., catalytic) puts the exploration of structure–property relationship on the same footing.

To obtain a more definitive picture of the atomic-scale structure of the studied Au NPs, we constructed real size and shape structure modes by reverse Monte Carlo simulations.¹¹

Finite size atomic configurations cut out from a perfect fcc lattice (see Figure S5 of the Supporting Information) were used to start the reverse Monte Carlo simulations. The configurations were spherical in shape and with the size of 3, 6, and 8 nm as the Au NPs studied here. In the simulations, the position of each atom from the 959, 6699, and 15 947 atom configurations, respectfully, was adjusted so as to minimize the difference R_w (see eq 3 above) between the model and experimental PDF data. Atoms were constrained (i) not to come closer than preselected distances of closest approach and (ii) to maintain as maximal (i.e., as close to 12) as possible coordination numbers. The first constraint reflects the fact that Au atoms in the NPs studied do not approach each other closer than 2.45 Å as the experimental Au PDFs show. The second constraint takes into account the close-packing nature of the atomic ordering in noble (Au) metals. At the same time, the energy of the configurations was optimized by minimizing pairwise (Lennard-Jones type) potentials for Au taken from literature sources.¹² The combined usage of constraints and potential minimization ensured a smooth convergence of the RMC simulations. They were done with the help of a new version of the program RMC++,¹³ expanding on our recent work.^{14,15}

The reverse Monte Carlo simulations refined structure models are shown in Figure 2. Not surprisingly, they fit the experimental atomic PDFs much better (see Figure 3) than the periodic, fcc lattice constrained models. The models resulted from the reverse Monte Carlo simulations show that the atomic ordering in 3–8 nm Au NPs is not uniform across their diameters. Atoms at the inner part of the NPs show fewer mean-square displacements than atoms closer to the NPs'

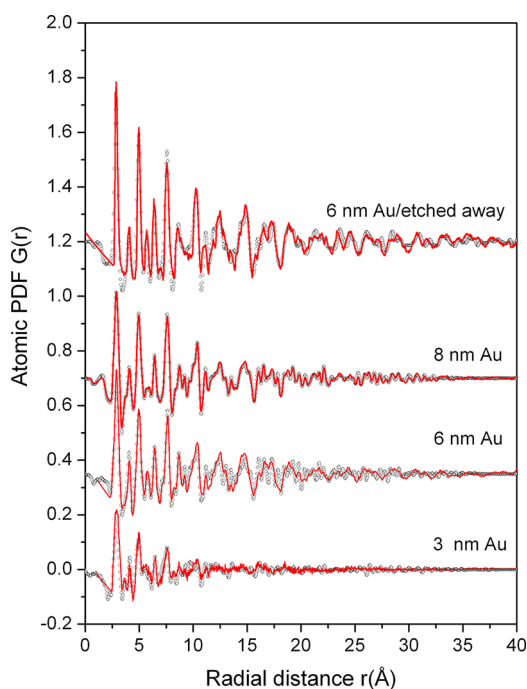


Figure 3. Experimental (symbols) and RMC fit (line) atomic PDFs for 3–8 nm Au particles. The goodness-of-fit factors for all data sets are on the order of 5–8%.

surface. Atoms at the surface may deviate from their average positions in a perfect fcc lattice by as much as 0.07Å^2 , mostly in a direction perpendicular to the NP's surface. This finding is fully in line with the results of other independent studies on NPs.¹⁶ The nonuniformity in the NP's atomic-scale structure may have important implications on their functional properties, in particular, the catalytic ones. In particular, because the NPs' surface is not terminated by families of flat atomic planes of a periodic fcc lattice but is uneven, the catalytic activity of NPs may be very different from that of the respective bulk solids.¹⁷

From the RMC constructed models for 3–8 nm Au particles, we computed not only two-atom correlation functions such as the PDFs but also three-atom correlation functions such as distributions of bond angles as well. The computations were done with the help of the program suite ISAACS.¹⁸ Bond angles are a very sensitive indicator of the type of local atomic ordering.^{19,20} Note that despite the presence of a substantial structural disorder, all NPs studied here have a well-defined local atomic ordering seen as a sequence of well-defined PDF peaks. (See Figure 1.) Computed bond-angle distributions for all atoms from the RMC produced atomic configurations (shown in Figure 2) and only for atoms from the top surface layer of the configurations are shown in Figure 4.

In a perfect fcc crystal (see Figure S5 of the Supporting Information), bond angles spike at 60, 90, 120, and 180°. In the etched 6 nm Au particles, bond angles show a distribution that is narrowly spread around the bond angles of a perfect fcc

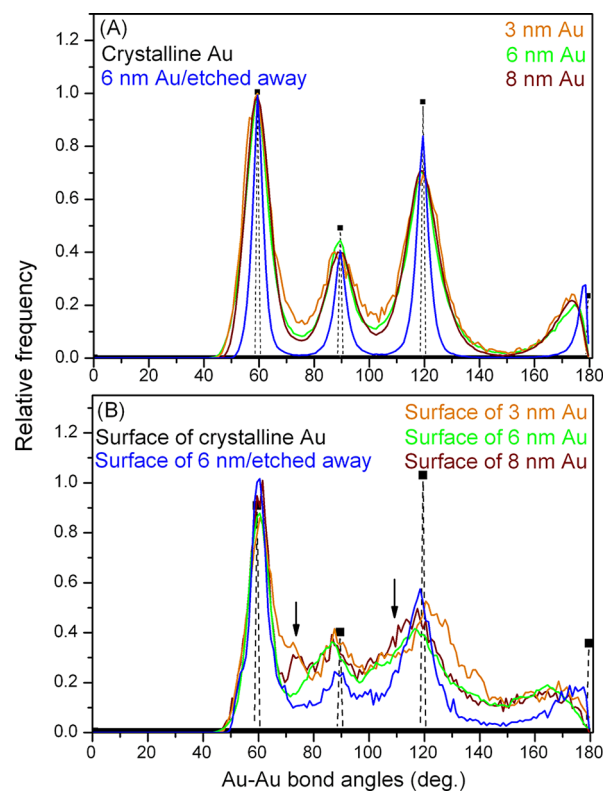


Figure 4. (A) Distribution of bond angles across 3–8 nm Au particles. (B) Distribution of bond angles in the top surface layer of 3–8 nm Au particles. The distributions are extracted from the RMC-generated structure models shown in Figure a2 and so represent an assembly averaged approximation to the bond angles distribution in real particles. Arrows mark the bond angles typical for noncrystallographic icosahedral atomic arrangement.

lattice, confirming the fcc character of the atomic-scale structure of these particles. Bond angles involving only atoms from the top surface layer show a broader distribution reflecting the presence of a substantial, surface introduced atomic positional disorder, yet the distribution is fairly symmetric about the bond angles of an fcc-type structure. Obviously atoms at the surface of the etched NPs also adopt an fcc-type ordering. The bond angles for the as-synthesized 3–8 nm particles show much broader distribution than those of the etched particles, revealing the presence of a much stronger structural disorder. This strong disorder is due to the fast reaction through which the former were obtained at close to room temperatures. Obviously the fast solution reaction has trapped the NPs in a more structurally disordered state. As a result, atoms at the surface of these NPs show extremely broad distributions of bond angles. These distributions have features not characteristic for the fcc-type structure. (See the arrows in Figure 4B.) In particular, bond angles at about 70 and 110° are characteristic of an icosahedral type atomic arrangement that has been observed with rapidly quenched from melt metallic glasses and quasi-crystals.^{19,20} Evidently, fast solution reactions are able to generate NPs with a heavily disordered atomic-scale structure that, especially close to the NPs surface, shows clear noncrystalline, icosahedral type features. Those features (compare the respective bond-angle distribution) appear strongest with the as-synthesized 8 nm particles, less strong with the 3 nm particles, and are weak but still clearly visible with the as-synthesized 6 nm particles. The catalytic activity of the as synthesized particles, which is mostly determined by how atoms at their surface are arranged,²¹ shows the same trend. (See Figure S3 of the Supporting Information.) It is best with the as-synthesized 8 nm particles, not as good with 3 nm particles, and even more diminished with the as-synthesized 6 nm. The etched 6 nm Au particles and the nanocrystalline commercial Au NPs come next in line. Obviously a strong correlation exists between the enhanced catalytic activity for ORR and the degree of icosahedral atomic arrangement in the Au NPs studied by us. This relationship may be summarized as *the higher the degree of icosahedrality, the better the activity for ORR in alkaline environment*.

Indeed, theory²² has long predicted the existence of noncrystallographic atomic arrangement in Au particles with a radius less than 10 nm. (See Figure 5.) Our studies provide strong evidence in support of these predictions. Independent confirmation of our findings comes from high-resolution TEM,⁵ showing the presence of noncrystallographic five-fold symmetry in 8 nm as-synthesized Au particles. (See Figure S6 of the Supporting Information.) Fragments from the surface of the RMC constructed models for the as synthesized and etched Au NPs are shown in Figure 6. Signatures of local five-fold symmetry are clearly seen in the former. For comparison, (100) and (110) facets from a fcc crystal that were found²¹ to exhibit a great difference in the catalytic activity for ORR are shown in the Figure as well. It is worth noting that a relationship between particles surface irregularity and activity as a function of size has been reported with small Pd particles as well.²³

4. CONCLUSIONS

In summary, depending on the particular technological route or the postpreparation treatment, nanosized catalysts may adopt substantially different atomic-scale structures (e.g., see Figure 2) and, hence, exhibit substantially different properties (e.g., see Figure S3 of the Supporting Information), even when their

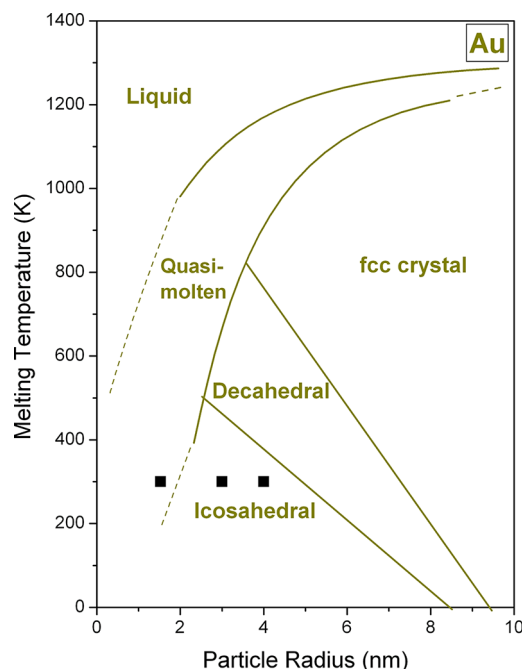


Figure 5. Theoretical phase diagram for nanosized Au (lines).²² Estimates for the effective radii (= NP's size/2) of the largely spherical in shape Au NPs studied by us are also given as solid squares.

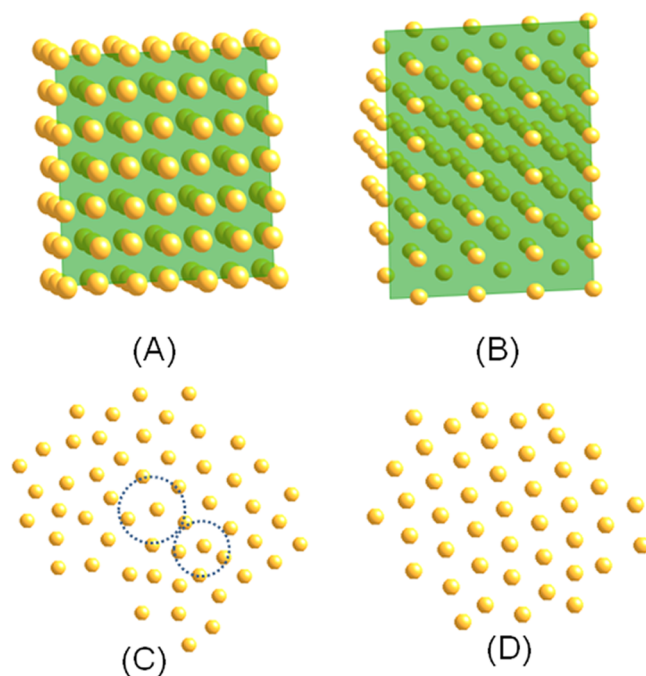


Figure 6. Fragments from a fcc crystalline lattice terminated with (A) highly catalytically active for ORR (100) and much less (B) active (110) atomic planes.²¹ Typical fragments from the surface layers of as synthesized (C) and etched Au NPs (D). Signatures of local structural disorder and five-fold symmetry (encircled) are well seen in the former but not in the latter.

composition and size/surface area are essentially the same. That is why the 3D structure of nanosized catalysts should be determined with due care and not assumed. Thanks to their high penetration depth and the ability to access high-Q values, high-energy XRD and PDF analysis coupled to computer simulations can determine the atomic-scale structure of NP

catalysts with any degree of crystallinity. (See Figure 2.) This would allow NPs' properties targeted for improvement to be considered in terms of a proper atomic-scale structure basis, be it of a "crystallographic" or "non-crystallographic" type, and so better understood. Also, structure models resulted from such experimental studies may serve as a basis for testing and improvement of the predictive power of theory and so help turn the still largely trial-and-error approach to developing of 1–10 nm sized materials into a smart engineering endeavor.

■ ASSOCIATED CONTENT

📄 Supporting Information

Synchrotron XRD patterns, TEM images, and catalytic activity data for the Au particles studied in this work. This material is available free of charge via the Internet at <http://pubs.acs.org>

■ AUTHOR INFORMATION

Corresponding Author

*E-mail: petko1vg@cmich.edu.

Notes

The authors declare no competing financial interest.

■ ACKNOWLEDGMENTS

Work shown in this article was supported by DOE-BES Grant DE-SC0006877. Work at the Advanced Photon Source was supported by DOE under Contract DE-AC02-06CH11357.

■ REFERENCES

- (1) Daniel, M. Ch.; Astruc, D. *Chem. Rev.* **2004**, *104*, 293–346.
- (2) Haruta, M.; Masakazu, D. *Appl. Catal., A* **2001**, *222*, 422–437.
- (3) Hvolbaek, B.; Janssens, T. V. W.; Clausen, B. S.; Falsig, H.; Christensen, C. H.; Norskov, J. K. *Nano Today* **2007**, *2*, 14–18.
- (4) Sun, Y.; Zhuang, L.; Lu, J.; Hong, X.; Liu, P. *J. Am. Chem. Soc.* **2007**, *129*, 15465–15467.
- (5) Lee, Y.; Loew, A.; Sun, S. *Chem. Mater.* **2010**, *22*, 755–61.
- (6) Petkov, V. *Mater. Today* **2008**, *11*, 28–38.
- (7) Egami, T.; Billinge, S. J. L. In *Underneath the Bragg Peaks*; Pergamon Press: Oxford, 2003.
- (8) Gilber, B.; Huang, F.; Zhang, H.; Waychunas, G. A.; Banfield, J. F. *Science* **2004**, *305*, 651–654.
- (9) Wyckoff, R. W. G. In *Crystal Structures*, 2nd ed.; Interscience Publishers: New York, 1963.
- (10) Farrow, C. L.; Juhás, P.; Liu, J. W.; Bryndin, D.; Božin, E. S.; Bloch, J.; Proffen, Th.; Billinge, S. J. L. *J. Phys.: Condens. Matter* **2007**, *19*, 335219-1–335219-7.
- (11) McGreevy, R. L.; Pusztai, L. *Mol. Simul.* **1998**, *1*, 359–367.
- (12) Heinz, H.; Vaia, R. A.; Farmer, B. L.; Naik, R. R. *J. Phys. Chem. C* **2008**, *112*, 17281–17290.
- (13) Gereben, O.; Jovari, P.; Temleitner, L.; Pusztai, L. *J. Optoelectron. Adv. Mater.* **2007**, *9*, 3021–3027.
- (14) Welborn, M.; Tang, W.; Ryu, J.; Crooks, R. M.; Petkov, V.; Henkelman, G. *J. Chem. Phys.* **2011**, *135*, 014503-1–014503-5.
- (15) Petkov, V.; R. Loukrakpam, R.; Yang, L.; Wanjala, B. N.; Luo, J.; Zhong, C. J.; Shastri, S. *Nano Lett.* **2012**, *12*, 4289–4299.
- (16) Huang, W. J.; Sun, R.; Tao, J.; Menard, L. D.; Nuzzo, R. G.; Zuo, J. M. *Nat. Mat.* **2008**, *7*, 308–313.
- (17) Sun, Ch.Q. *Nanoscale* **2010**, *2*, 1930–1961.
- (18) Roux, S. L.; Petkov, V. *J. Appl. Crystallogr.* **2010**, *43*, 181–184.
- (19) Hafner, J.; Krajci, M. *Europhys. Lett.* **1990**, *13*, 335–40.
- (20) Steinhardt, P. J.; Nelson, D. R.; Ronchetti, M. *Phys. Rev. B* **1983**, *28*, 784–805.
- (21) Schmidt, T. J.; Stamenovic, V.; Arez, M.; Marcovic, N. M.; Ross, P. N. *Electrochim. Acta* **2002**, *47*, 3765–3776.
- (22) Marks, L. D. *Rep. Prog. Phys.* **1994**, *57*, 603–659.
- (23) Coppage, R.; Slocik, J. M.; Briggs, B. D.; Frenkel, A. I.; Heinz, H.; Naik, R. R.; Knecht, M. R. *J. Am. Chem. Soc.* **2011**, *133*, 12346–12349.